1684

Upconversion-Induced Heat Generation and Thermal Lensing in Nd:YLF and Nd:YAG

M. Pollnau*, P. J. Hardman, M. A. Kern,
W. A. Clarkson, and D. C. Hanna

Optoelectronics Research Centre
University of Southampton
Southampton SO17 1BJ
United Kingdom

*Present Address:
Department of Chemistry and Biochemistry, University of Bern
Freiestrasse 3, CH-3012 Bern, Switzerland
phone ++41-31-631 42 53, Fax ++41-31-631 43 99
e-mail pollnau@iac.unibe.ch

submitted to Phys. Rev. B
28/5/98

1. Introduction

The Nd:YAG ($Nd^{3+}:Y_3Al_5O_{12}$) and Nd:YLF ($Nd^{3+}:LiYF_4$) transitions at 1.064 µm and 1.053 µm, respectively, have been widely used for laser applications, because they offer several advantages over other laser systems: The Nd^{3+} transition at 1 µm involves a four-level scheme with fast multiphonon transitions populating the upper and depleting the lower laser level. Its large stimulated-emission cross-section allows a low laser threshold, while the small quantum defect allows high slope efficiency. YAG has a high fracture limit which is of advantage for use in high-power laser systems. YLF, on the other hand, is an attractive host material because of the wavelength match of the laser transition (1.053 µm) with Nd^{3+} glass amplifiers, the long storage time of the Nd^{3+} upper laser level, its natural birefringence, and its relatively weak thermal lensing on the polarization corresponding to 1.053 µm operation [1]. This weak lensing observed under lasing conditions is a consequence of YLF showing a decrease of refractive index with increasing temperature, creating a negative thermal lens, which partly compensates for the positive lens due to the bulging of the rod end faces. It gives Nd:YLF a significant advantage over Nd:YAG for power-scaling of diode-end-pumped systems into the multiwatt region while retaining an output beam of high spatial quality [2, 3, 4].

However, under conditions of higher excitation density, such as non-lasing conditions, Q-switched operation, or operation as an amplifier, a strong deterioration in the performance of this seemingly simple system is observed. With increasing pump power and intensity, the Nd:YLF system exhibits a significantly reduced storage time under Q-switched operation and a decreasing laser efficiency [5, 6, 7]. This behavior has been explained by lifetime quenching owing to interionic upconversion processes involving two neighboring ions in the upper laser level [8, 9, 10]. As a consequence, Nd:YLF exhibits visible fluorescence from energy levels above the pump level. Furthermore, measurements of the induced thermal lens under lasing and non-lasing conditions demonstrate that significant additional heat is generated in the non-lasing situation, with the same pump power [11]. For Nd:YAG, similar effects of fluorescence quenching [12, 13], additional heat generation [14, 15], and increased thermal lensing [16] under non-lasing conditions have been observed.

Appendix A and the equations implemented in the computer program are introduced in Appendix B.

2. Population Dynamics

Detailed measurements of the thermal lensing behavior versus pump power under lasing and non-lasing conditions revealed that there is a significant increase in thermal lens powers under non-lasing compared to lasing conditions, with up to a factor of six observed in Nd:YLF [11] and up to a factor of two in Nd:YAG [16]. To investigate this behavior, a computer source code was developed that allowed the three-dimensional calculation of heat generation, heat conduction, temperature distribution, and thermal lensing on the basis of the spatially resolved population dynamics of the system. The specific experimental situations referred to above [11, 16] are the starting points of our numerical investigations.

In a computer simulation involving the relevant levels (ground state and eight excited states, see Fig. 1) and processes (pump power and configuration, ground-state absorption and depletion, all lifetimes and branching ratios, three interionic processes, stimulated emission, and the data of crystal and resonator), time- and space-dependent rate equations describing the Nd:YLF and Nd:YAG systems are solved numerically in order to obtain a quantitative understanding of our experimental results. For the tetragonal YLF system, a three-dimensional (tangential, sagittal, longitudinal) resolution is chosen, whereas the calculations for the cubic YAG system are performed with two-dimensional (radial, longitudinal) resolution. In these simulations the population dynamics are calculated and the heat generation, temperature distribution, and consequent thermal lensing behavior under lasing and non-lasing conditions are investigated.

In the experiments the radiation of a 20-W diode-laser bar was focused onto the crystal front surface, using a beam-shaping technique [28]. Pump details and details of laser mode size are given in Tables 1 and 4 in Appendix A, respectively. The pump radiation was absorbed on the ground-state transition $^4I_{9/2} \rightarrow {}^4F_{5/2}$, see Fig. 1. The spectral distribution of the pump radiation is taken into account in the simulation. The spectral line shape is treated as Gaussian. The absorption cross-sections in Nd:YLF are taken from the spectrum of Fig. 2. In our

Interionic upconversion has been discussed in recent papers as a source of lifetime quenching in Nd:YLF under conditions of high excitation density [8, 9, 10]. Three upconversion processes UC_1-UC_3 (see Fig. 1) have been suggested [10] to contribute in a significant way to the population dynamics in Nd:YLF. These processes are considered in our simulation. The measured value for the parameter describing the influence of these combined upconversion processes, namely 1.7×10^{-16} cm^3/s [8], was confirmed in an independent approach [10], but with relatively high error margin. The estimated parameters of the individual interionic upconversion processes are given in Table 3 of Appendix A. The investigations of Ref. [10] indicate that the spectral overlap of the upconversion processes UC_1-UC_3 does not vary significantly with temperature in the range 250-500 K, hence a possible temperature dependence of the parameters of upconversion is not considered in the simulations.

Investigation of interionic upconversion in Nd:YAG [8, 34] resulted in published parameters which vary significantly in value. The value of the upconversion parameter of 5×10^{-17} cm^3/s (6900 s^{-1} for a dopant concentration of 1 at.%) determined in Ref. [34] was found to provide consistency of our experimental and calculated results for thermal lens powers.

It is apparent from Fig. 1 that, since levels 1 to 3 and 5 to 8 decay predominantly via fast multiphonon relaxation into their next lower-lying levels [10] and have a population density of $<10^{-6}$ of the dopant concentration, the effect of the three different processes UC_1-UC_3 on the population dynamics is similar (cf. the detailed discussion in Ref. [10]). It is, therefore, of no great importance for our calculation which parameters of the individual upconversion processes are actually used in the rate equations as long as the sum of the parameters is equal to the parameters published for Nd:YLF [8, 10] and Nd:YAG [34] (cf. also Section 3 for the influence of upconversion on heat dissipation).

The population densities of the levels which are denoted by a number and a spectroscopic term as well as the excitation and relaxation rates indicated in Fig. 1 are calculated from the rate-equation system (7)-(15) of Appendix B, using the spectroscopic parameters of Table 3 of Appendix A. The spatially resolved stimulated-emission rate on the laser transition $^4F_{3/2} \rightarrow {}^4I_{11/2}$, see Fig. 1, is calculated from eqs. (16)-(19) of Appendix B, using the parameters of Table 4 of Appendix A.

quadratic dependence on excitation density, is two orders of magnitude larger under non-lasing conditions compared to lasing conditions (Fig. 4).

Comparison of the upconversion rate with the pump rate provides an indication of the absolute influence of upconversion. The upconversion rate is defined here as the rate for a single ion, i.e. the depletion rate of the $^4F_{3/2}$ level population is twice this rate. Under non-lasing conditions, on the one hand, the upconversion rate reaches 63% in the center of the pump beam at the highest pump power. This means that the depletion rate of the $^4F_{3/2}$ level by upconversion is 126% of the pump rate, which is possible, because the half of the population which is upconverted to high-lying levels subsequently repopulates the $^4F_{3/2}$ level via multiphonon relaxation, thus introducing an additional excitation rate for this level of 63% of the real pump rate. Under lasing conditions, on the other hand, interionic upconversion has a marginal influence.

The additional depletion rate which is introduced to the $^4F_{3/2}$ upper laser level by interionic upconversion leads to a significant decrease in the lifetime of this level. Consequently, this reduces the storage capacity of the system under Q-switched operation or operation as an amplifier. This effect has been discussed in detail in Refs. [8, 10].

3. Heat Generation and Temperature Profiles

The main purpose of our investigation is to understand the non-linearities which lead to the strong difference in thermal lens power measured under lasing and non-lasing conditions [11, 16]. In this section, the processes that lead to heating of the Nd:YLF and Nd:YAG crystals are identified and the spatial temperature profiles are derived.

3.1. Heat Generation

It is assumed in our calculation that pump absorption and fluorescent emission do not contribute directly to thermal loading of the rod by intra-multiplet phonon relaxation, i.e., the actual Stark-level structures are neglected and the transitions are assumed to originate from and terminate in the lowest Stark levels of the corresponding multiplets. Thus, these processes contribute only threshold is low. This finding is in agreement with the result obtained from the solution of the full rate-equation system, see Fig. 5, which is 2.3 W of thermal load for 9.5 W of absorbed power in Nd:YLF.

Under non-lasing conditions, the situation is much more complicated. When calculating the heat generated by the linear relaxation rates, the branching ratios from the $^4F_{3/2}$ level (see Table 3 of Appendix A) have to be taken into account. In Nd:YLF, a fraction of $\gamma_{43}\ \beta_{43} = 0.034$ is assumed to decay via multiphonon relaxation from the upper laser level to the next lower-lying level and further via multiphonon processes to the ground state, i.e., all four processes $^4F_{3/2} \rightarrow {}^4I_{15/2} \rightarrow {}^4I_{13/2} \rightarrow {}^4I_{11/2} \rightarrow {}^4I_{9/2}$ generate heat in this case. This rate includes the part that decays via cross relaxation. A fraction of $(1 - \gamma_{43})\ \beta_{43} = 0.121$ decays via fluorescence on the transition $^4F_{3/2} \rightarrow {}^4I_{15/2}$ and generates heat only via the latter three processes, a fraction of β_{42} decays via fluorescence on the transition $^4F_{3/2} \rightarrow {}^4I_{13/2}$ and generates heat via the latter two processes etc. This results in the relative strengths of the above four processes as indicated in Table 5 of Appendix A. When neglecting interionic processes, the result is that 25% of absorbed pump power would be converted to heat, which is similar to the fraction under lasing conditions.

The same investigation in Nd:YAG leads to a similar fraction of 25% under lasing conditions, but the corresponding fraction of heat generation owing to linear processes under non-lasing conditions would increase to more than 29%. This is because of the larger phonon energies in YAG as well as additional non-radiative quenching channels [12, 13, 15, 29, 30, 32, 33], resulting in an increased non-radiative rate from the $^4F_{3/2}$ upper laser level and a correspondingly smaller fluorescence lifetime in Nd:YAG.

However, the upconversion processes lead to a relative increase in the rates of the multiphonon processes compared to predominantly fluorescent decay and, in addition, induce the processes $^2G(1)_{9/2} \rightarrow {}^4G_{7/2} \rightarrow {}^4G_{5/2} \rightarrow {}^4F_{5/2} \rightarrow {}^4F_{3/2}$. Therefore, the heat dissipation calculated from the full rate-equation system under non-lasing conditions deviates significantly from the values of 25% in Nd:YLF or 29% in Nd:YAG, see Fig. 5, and increases non-linearly with pump power. In Nd:YLF, 4.9 W of thermal load for 9.5 W of absorbed pump power is generated under non-lasing conditions, i.e. 52% or more than twice the amount of heat compared to lasing conditions. The result for Nd:YAG, 40% or 5.4 W of thermal load for 13.5 W of

115 K at the point of highest pump absorption, see Fig. 6a. Consequently, the temperature gradient is much more pronounced under non-lasing conditions.

The corresponding temperature increase in Nd:YAG for 9.5 W of absorbed power is only 37 K and 62 K under lasing and non-lasing conditions, respectively. At the highest absorbed power of 13.5 W, the increase is 54 K and 95 K, respectively. The larger temperature increase in Nd:YLF is a result of the smaller thermal conductivity in this host and the larger contribution of upconversion under non-lasing conditions. The temperature dependence of the thermal conductivity further increases the temperature in the Nd:YLF rod.

We include the spectral distribution of the diode pump power in our calculation, cf. eqs. (1)-(6) of Appendix B and Table 2 of Appendix A. Since the absorption cross-section changes with pump wavelength, the absorption length may vary significantly over the spectral pump distribution. In Nd:YLF, the pump wavelength was significantly detuned from the absorption peak at 797 nm, see Fig. 2, in order to prevent rod fracture.

Now we consider a situation where the spectral emission of the diode pump power is temperature tuned by only 0.2 nm toward the absorption peak at 797 nm (dashed line in Fig. 2). Since the major part of the pump power is in a spectral region where the absorption cross-section changes only slightly with pump wavelength, the total absorption of the incident pump power of 12 W increases only from 79% to 80% under non-lasing conditions. This is a tiny effect and would hardly be noticed in a direct way in the experiment, but the consequences for temperature, stress, and strain in the rod are much more pronounced. A small part of the pump power at the short-wavelength side of the pump spectrum is shifted to a wavelength region of strong absorption, cf. Table 2 of Appendix A, and is now absorbed within the front part of the crystal. The calculation shows that, with all the non-linearities involved, the temperature in Nd:YLF at the front surface in the center of the pump beam increases from 404 to 414 K, thus strongly increasing stress and strain in this area and, ultimately, posing an increased risk of rod fracture.

the Debye function. The measured temperature dependence of the expansion coefficient in YAG is in reasonable agreement with this model. Again, temperature-dependent data were not available for YLF and the dependence is estimated from the data available for YAG, which is justified by the model. For details, cf. Appendix A and eqs. (28) and (29) of Appendix B.

The third effect, the stress-induced birefringence, is not considered in our calculation. It is believed to be of minor importance in YLF [23], because this material shows a strong natural birefringence.

Stress and strain also have an influence on the expansion of the crystal. Equation (29) of Appendix B as well as the data of the expansion coefficient presented in Appendix A rely on the free expansion of the crystal in one direction. If a transversely localized temperature increase occurs (e.g. end-pumping with a Gaussian profile), the heated element cannot freely expand in longitudinal direction, because it is constrained by its colder surrounding. We make the simplifying assumption that eq. (29) of Appendix B is modified by stress and strain to eq. (30), where the parameter C_α takes account of this constraint. The above assumption results in the contribution of the bulging having the same radial dependence as the temperature distribution. In practice, the shape of the bulge will probably differ from this profile due to the modifications introduced by stress and strain, but this first-order approximation is more realistic than assuming free expansion.

C_α is treated as the only free parameter in all the calculations presented in this paper. It is adjusted in order to match a single measured value, the value of the thermal lens power at highest pump power under non-lasing conditions in π-polarization along the YLF a-axis. It is kept at a constant value for all calculations. This does not introduce a general degree of freedom to the calculations, as will become apparent later from Fig. 7a: Since the contributions to thermal lensing due to the change in refractive index and bulging have opposite signs and since the former exceeds the latter for π-polarization, but the reverse is true for σ-polarization, resulting in thermal lenses of opposite sign for π- and σ-polarization, the variation of C_α does not allow for an adjustment of the calculated magnitude of the thermal lens power in both π- and σ-polarizations. With increasing C_α the thermal lens becomes stronger in σ-polarization, but it simultaneously becomes weaker in π-polarization and vice versa. In addition, a fixed value of C_α has no direct parameters lead to a thermal lens whose power increases non-linearly with pump power. At the highest pump power of 12 W, the thermal lens power under non-lasing conditions compared to lasing conditions is almost six times stronger in π-polarization and almost five times stronger in σ-polarization. The difference in this factor for the two polarizations is a consequence of the different temperature dependence of the change in refractive index and thermal expansion coefficient. The agreement between experimental and calculated results is excellent, indicating that the major contributions to heat generation and thermal lensing for the a-axis have been identified.

The measured thermal lens power parallel to the c-axis (tangential plane) is much weaker than that perpendicular to the c-axis (sagittal plane) [11], which is partly due to the larger pump-waist radius in the tangential resonator plane (340 μm compared to 220 μm in the sagittal plane) and partly due to reasons yet unknown to us. The measured thermal lens power parallel to the c-axis is less accurately reproduced in the simulation, with the calculated values being larger than the measured values.

A possible reason for the difference in thermal lens powers along the two crystal axes could be a much larger difference in the thermal conductivity for a- and c-axis than reported in Ref. [38]. When treating the thermal conductivity in a- and c-axis direction as free parameters, we find from our calculations that the thermal conductivity along the c-axis must be more than a factor of two larger than along the a-axis in order to reproduce the difference in thermal lens powers as obtained from the measurements. A single influence of either the change of refractive index with temperature or the bulging of the rod end faces can be excluded as a reason, because it would lead to thermal lens values which are more positive or negative for both π- and σ-polarization. The experimental results [11] show instead a decrease of the absolute values for both π- and σ-polarization.

The experimental results (solid symbols) of Ref. [16] and calculated results (open symbols) for Nd:YAG are shown in Fig. 8a. Since the YAG system is cubic, the behavior for tangential and sagittal planes as well as for the corresponding polarizations are identical, and the behavior is described by only one curve for lasing condition and one for or non-lasing.

to a dramatic change in the behavior of the laser system. A proper resonator design which avoids even small resonator losses is, therefore, of extreme importance in order to operate such a laser at high output power in a transversely fundamental mode.

4.3. Consequences for Certain Operational Regimes

It becomes apparent from the investigations of this paper that the problems of heat generation, thermal lensing, and lens aberration increase significantly, if the system is operated in a regime of higher excitation density, i.e. in a Q-switched regime, as an amplifier, or on a low-gain transition, because upconversion plays a larger role in these regimes, with all the consequences discussed above.

Generally the best way to limit the influence of interionic upconversion is to use a smaller dopant concentration. This decreases energy migration within the initial level of the upconversion process and hence the possibility of two excitations to meet at nearest-neighbor distance. Thus, the upconversion parameter decreases. In addition, the excitation density under the same pump conditions is smaller. However, this measure implies that a longer rod is used in order to maintain the fraction of pump power which is absorbed in the rod. If also the absorbed pump intensity is a critical parameter, this requires a pump source with correspondingly high brightness, i.e. small M^2 values.

A second possibility which underlies the same restriction concerning the pump source is to tune the pump to a wavelength with smaller absorption cross-section, which also decreases the excitation density. This measure is less powerful than the first, because it does not simultaneously decrease the upconversion parameter. Thirdly, the influence of upconversion can also be decreased by focusing to a larger pump-waist size.

Under Q-switched operation, where the pump intensity is less critical, all these methods can be applied. When operating the system as an amplifier, a high pump intensity is essential for efficient amplification. The pump beam cannot be defocused and a high-brightness pump source is essential in order to apply one of the first two methods. Since no stable resonator has to be established for the signal beam, the quenching of the storage time of the $^4F_{3/2}$ level by

Interionic upconversion processes from the $^4F_{3/2}$ level and subsequent cascaded multiphonon relaxation were found to be responsible for a significant increase in heat generation in Nd:YLF from 24% of the absorbed pump power under lasing conditions up to 52% under non-lasing conditions, for a maximum absorbed pump power of 9.5 W. In Nd:YAG, corresponding values are 25% and 40%, for 13.5 W of absorbed pump power. The additional heat load increases non-linearly with pump power. Taking into account the unfavorable temperature dependence of the thermal conductivity, this leads to an increase in temperature in Nd:YLF at the point of highest pump absorption from 332 K under lasing conditions to 404 K under non-lasing conditions, when setting the coolant temperature to 288 K. Corresponding temperature values in Nd:YAG are 342 K and 383 K, respectively. Owing to the spectral distribution of the diode pump power, tuning of the diode emission wavelength may lead to a significant increase in temperature, stress, and strain. Thus small changes in the overall absorbed pump power can lead to significantly worsened risk of rod fracture.

Thermal lens powers were calculated in Nd:YLF for the crystal a- and c-axis direction and for π- and σ-polarization under lasing and non-lasing conditions. For the a-axis, calculated results are in excellent agreement with experimental data. The thermal lens power depends almost linearly on pump power under lasing conditions, whereas, under non-lasing conditions, a strongly non-linear behavior is measured and calculated, caused by upconversion as well as the temperature dependence of thermal and thermo-optical parameters. Thermal lens powers up to a factor of six larger were observed under non-lasing compared to lasing conditions. The significantly weaker thermal lensing for the crystal c-axis has as yet not been understood. The temperature dependence of the thermal and thermo-optical parameters as well as the components of the strain and elasto-optical tensors will have to be measured accurately and the thermally induced stress and strain will have to be included in the simulation in order to provide a more detailed understanding of thermal lensing in the YLF host.

In Nd:YAG, the observed increase in thermal lens power from lasing to non-lasing conditions was only a factor of two because of the stronger linear decay rates and the smaller upconversion parameter compared to Nd:YLF. However, thermal lens powers are generally higher than in Nd:YLF, because in YAG the change in refractive index with temperature is larger and the

Appendix A: Parameters and Values

This appendix explains all parameters which are relevant for the computer calculations and provides all values used in the simulations.

In Table 1, the data of the Nd:YLF and Nd:YAG crystals as well as the data of the pump beams are summarized. Absorbed fractions of the launched pump power at low input power are experimental data which are reproduced in the calculations. Absorbed fractions at high pump power are determined from the calculations and take into account ground-state bleaching. M^2 values of the pump beam in the Nd:YAG experiment are averaged from the values measured along the tangential and sagittal planes.

Table 2 provides the spectral distribution of the diode pump power in the experiments investigating Nd:YLF (upper 8 rows) and Nd:YAG (lower 5 rows). The temperature-stabilized pump wavelengths are centered at λ_p = 800.1 nm and λ_p = 809.0 nm, respectively. The spectral line widths are approximately $\Delta\lambda$ = 3 nm. For the simulations, the spectral pump shape is assumed to be Gaussian, and 8 (or 5) individual spectral parts centered at wavelength $\lambda(i)$ are calculated. Also given are the fractional power $P_{in,\lambda(i)} / P_{in}$ and the absorption cross-section $\sigma_{p,\lambda(i)}$ of each part, as derived from the spectrum of Fig. 2 (Nd:YLF) or from the corresponding spectrum of Nd:YAG. If, in the Nd:YLF experiment, the diode is temperature-tuned by $\Delta\lambda_s$ = 0.2 nm toward the absorption peak at 797 nm, the individual absorption cross-sections are shifted toward the values $\sigma_{s,\lambda(i)}$.

In Table 3, the spectroscopic parameters of Nd:YLF and Nd:YAG are presented. The intrinsic lifetimes of upper and lower laser level are given in the Table. The lifetimes τ_i of the other excited levels have been discussed in Ref. [10] for Nd:YLF and are assumed here as τ_i ~ 20 ns for Nd:YLF and Nd:YAG. The branching ratios β_{4i} from the ${}^4F_{3/2}$ upper laser level are calculated from Judd-Ofelt data for the radiative transition rates in Nd:YLF [47] and Nd:YAG [48] and from the fluorescence lifetime τ_4 with the procedure used in Ref. [49]. This procedure assumes that the difference between the total intrinsic decay rate τ_4^{-1} and the sum of the radiative decay rates is due to multiphonon relaxation into the next lower-lying level ${}^4I_{15/2}$. The nonradiatively emitted fraction of the rate from the ${}^4F_{3/2}$ upper laser level into the next lower-lying level is given by γ_{43}, from crystal via copper to water and 6.5 W K^{-1} m^{-2} for heat transfer from crystal to air in our calculations.

The refractive index n_r is taken from Refs. [23, 24, 39, 42]. Published data of the change in refractive index with temperature, $n_r' = dn_r / dT$, at room temperature are 7 [2], 7.2 [40], 7.3 [23, 39], 8.3 [24], 8.9 [38], and 9.86×10^{-6} K^{-1} [42, 21]. We use the value of Ref. [24], because this Ref. provides temperature-dependent data, from which we calculate the value of $n_r'' = dn_r' / dT = 2.6\times10^{-8}$ K^{-2}.

Room-temperature data of the expansion coefficient α_T' are 5.8 [35], 6.7 [38], 6.95 [40], 7-8 [2], 7.3-7.7 [43], 7.5 [24, 53], 7.7-8.2 [39], 8.2 [23], and 8.9×10^{-6} K^{-1} [54]. We use the recently published value of Ref. [35], because this Ref. provides temperature-dependent data, from which we calculate the value of the almost linear increase of α_T' with temperature of $\alpha_T'' = d\alpha_T' / dT = 1.25\times10^{-8}$ K^{-2} (cf. the value of 1.625×10^{-8} K^{-2} derived from the data of Refs. [24, 39]). Published values of Poisson's ratio are 0.25 [35] and 0.30 [23].

In the model of Ref. [36], the expansion coefficient is proportional to the Grüneisen parameter and the specific heat which both depend on temperature. Since the Grüneisen parameter increases only slightly for temperatures approaching the Debye temperature T_D (750 K in YAG [37, 43]), the temperature dependence of the expansion coefficient is mostly determined by the temperature dependence of the specific heat, which is given by the Debye function. At room temperature or 0.4 T_D, the Debye function increases with a slope of 1.4×10^{-3} K^{-1}, in reasonable agreement with the value of $\alpha_T'' / \alpha_T' = 2.2\times10^{-3}$ K^{-1} derived from the data of Ref. [35]. The remaining part can be attributed to the temperature dependence of the Grüneisen parameter.

Values of the thermal conductivity in YLF [38], measured in a- and c-axis direction at room temperature, of K_{Ca} = 7.2 W/Km and K_{Cc} = 5.8 W K^{-1} m^{-1}, respectively, are used in the calculation (cf. the value of K_C = 6 W K^{-1} m^{-1} [2, 23, 39, 55], with no indication of a dependence on crystal axis given in those Refs.). Values of $n_r' = dn_r / dT$ at T_0 = 300 K, for the two crystal axes in YLF, are $n_{rc}'(T_0) = -4.3\times10^{-6}$ K^{-1} and $n_{ra}'(T_0) = -2.0\times10^{-6}$ K^{-1} [2, 23, 38] (c.f. the values of $n_{rc}'(T_0) = -3.0\times10^{-6}$ K^{-1} and $n_{ra}'(T_0) = -0.8\times10^{-6}$ K^{-1} [55]).

Several temperature-dependent data of YLF could not be found in literature. These values are estimated from the corresponding temperature dependence in YAG and are denoted with an

The geometry of the spatial resolution is denoted by $\mathbf{r} = (x, y, z)$, the space vector, $r = (x, y)$, its transverse part, $x_1(r)$, $y_1(r)$, and $x_2(r)$, $y_2(r)$, the inner and outer transverse borders of the spatial element, its lengths $\Delta x(r) = x_2(r) - x_1(r)$ and $\Delta y(r) = y_2(r) - y_1(r)$, $\Delta\ell(z)$, the length of the longitudinal element z, and $Vol(\mathbf{r}) = \Delta x(r)\ \Delta y(r)\ \Delta\ell(z)$, the volume of the spatial element at $\mathbf{r}$. $\Delta\bar{x}(rr')$, $\Delta\bar{y}(rr')$, and $\Delta\bar{\ell}(zz')$ are the distances between the centers of adjacent spatial elements located at $\mathbf{r}$ and $\mathbf{r}'$.

B.1. Rate Equations

The absorption coefficients $\alpha_{\lambda(i)}(\mathbf{r})$ of the individual spectral parts i of the pump beam at wavelength $\lambda(i)$ within the spatial element at $\mathbf{r}$ are

$$\alpha_{\lambda(i)}(\mathbf{r}) = \sigma_{p,\lambda(i)} N_0(\mathbf{r}), \tag{1}$$

where $N_0(\mathbf{r})$ is the population density of the ground state. The pump-beam radii in tangential and sagittal resonator plane (with the waist radii w_{px0} and w_{py0} at the crystal front surface $z = 0$) are given by

$$w_{px/y}(z)^2 = w_{px0/y0}^2 + \left[\frac{z\, M^2_{x,y}\, \lambda_p}{\pi\, n_{rc/a}\, w_{px0/y0}}\right]^2, \tag{2}$$

The fraction $\rho_p(\mathbf{r})$ of the power of the Gaussian pump beam contained in the spatial element at $\mathbf{r}$ compared with the total pump power in the longitudinal element z is

$$\rho_p(\mathbf{r}) = \frac{2}{\pi\, w_{px}(z)\, w_{py}(z)} \int_{x_1(r)}^{x_2(r)} \exp\left(\frac{-2\, x'^2}{w^2_{px}(z)}\right) dx' \int_{y_1(r)}^{y_2(r)} \exp\left(\frac{-2\, y'^2}{w^2_{py}(z)}\right) dy'. \tag{3}$$

$$dN_5(r)/dt = R_{05}(r) - \tau_6^{-1} N_6(r) - \tau_5^{-1} N_5(r) \tag{10}$$

$$dN_4(r)/dt = \tau_5^{-1} N_5(r) - \tau_4^{-1} N_4(r) - 2\,(W_1 + W_2 + W_3)\, N_4^2(r) - SE_{\pi/\sigma}(r) \tag{11}$$

$$dN_3(r)/dt = \beta_{43}\, \tau_4^{-1} N_4(r) - \tau_3^{-1} N_3(r) + W_1 N_4^2(r) \tag{12}$$

$$dN_2(r)/dt = \beta_{42}\, \tau_4^{-1} N_4(r) + \tau_3^{-1} N_3(r) - \tau_2^{-1} N_2(r) + W_2 N_4^2(r) \tag{13}$$

$$dN_1(r)/dt = \beta_{41}\, \tau_4^{-1} N_4(r) + \tau_2^{-1} N_2(r) - \tau_1^{-1} N_1(r) + W_3 N_4^2(r) + SE_{\pi/\sigma}(r) \tag{14}$$

$$N_d = \sum_{i=0}^{8} N_i(r). \tag{15}$$

For the calculation of the stimulated-emission rate, the following considerations are made. Thermal redistribution within the multiplets takes place instantaneously. Since the temperature profile of the active material is calculated in the simulation, the Boltzmann distributions of upper and lower Stark laser levels are considered with spatial resolution. The fraction $\rho_l(r)$ of the photon number of the Gaussian laser beam contained in the spatial element at r compared with the total photon number in the longitudinal element z is

$$\rho_l(r) = \frac{2}{\pi\, w_{lx}(z)\, w_{ly}(z)} \int_{x_1(r)}^{x_2(r)} \exp\left(\frac{-2\,x'^2}{w_{lx}^2(z)}\right) dx' \int_{y_1(r)}^{y_2(r)} \exp\left(\frac{-2\,y'^2}{w_{ly}^2(z)}\right) dy'. \tag{16}$$

In the low-gain approximation, the rate equation for the photon number $\phi_{\pi/\sigma}$ in the resonator for π- and σ-polarization, respectively, is given by

$$d\phi_{\pi/\sigma}/dt = \frac{\ell_c}{\ell_{opt}} \sum_{z=1}^{n} \left\{ \sum_{x,y=1}^{m} \left[P\, \beta_{41}\, \tau_4^{-1} N_4(r) + SE_{\pi/\sigma}(r) \right] Vol(r) \right\}$$

$$- \left\{ -\ln\left[Rf_1\, Rf_2\, (1-L) \right] \right\} \frac{c}{2\,\ell_{opt}}\, \phi_{\pi/\sigma}\,, \tag{17}$$

$$P_{th,y}(\mathbf{r}) = -K_{Ca}(T(\mathbf{r}))\, \Delta\ell(z)\, \Delta x(r)\, [\Delta T_y(\mathbf{r}'\mathbf{r}) / \Delta\bar{y}(r'r) - \Delta T_y(\mathbf{r}\mathbf{r}'') / \Delta\bar{y}(rr'')] \qquad (22)$$

$$P_{th,z}(\mathbf{r}) = -K_{Ca}(T(\mathbf{r}))\, \Delta x(r)\, \Delta y(r)\, [\Delta T_z(\mathbf{r}'\mathbf{r}) / \Delta\bar{\ell}(z'z) - \Delta T_z(\mathbf{r}\mathbf{r}'') / \Delta\bar{\ell}(zz'')] \qquad (23)$$

and with eq. (20), the equation for the thermal conduction [56] reads

$$\partial T(\mathbf{r})/\partial t = \frac{1}{C_p\, \rho\, \mathrm{Vol}(\mathbf{r})} [Q_{th}(\mathbf{r}) + P_{th,x}(\mathbf{r}) + P_{th,y}(\mathbf{r}) + P_{th,z}(\mathbf{r})]. \qquad (24)$$

Here $\Delta T(\mathbf{r}'\mathbf{r})$ is the difference between the temperatures $T(\mathbf{r}')$ and $T(\mathbf{r})$ at the centers of two adjacent spatial elements at $\mathbf{r}'$ and $\mathbf{r}$, respectively, in the direction ($\mathbf{r}' \rightarrow \mathbf{r}$) of the power $P_{th}(\mathbf{r})$ of the thermal flux. The convention for the sign of $\Delta T(\mathbf{r}'\mathbf{r})$ is such that power $P_{th}(\mathbf{r})$ flowing into the spatial element at $\mathbf{r}$ has a positive sign. At room temperature and above, the temperature dependence of the thermal conductivity of a crystalline material is sufficiently well described by the general law [36]

$$K_{Cc/a}(T(\mathbf{r})) = \Theta_{c/a}\ T^{\delta}(\mathbf{r}), \qquad (25)$$

where the parameter δ depends on the host material and is usually in the range [1...2]. Experimental results for YAG (c.f. Refs. [22, 57] and Refs. in there) suggest $\delta \approx 1$ around 300 K. This value is also used as an approximation in our calculation for YLF. Radial convective cooling by a water-cooled copper heat sink and convective air cooling at the rod end faces is assumed. The radial and longitudinal boundary conditions are [20, 26, 56]

$$\partial T(\mathbf{r})/\partial n_{r/z} = \frac{K_{Tr/z}}{K_{Cc/a}(T(\mathbf{r}))} [T(\mathbf{r}) - T_{br/z}], \qquad (26)$$

Here C_α is a parameter varying in the range [0...1]. It takes into account that, if a transversely localized temperature increase occurs, the heated element cannot freely expand in longitudinal direction, because it is constrained by its colder surrounding.

The change in refractive index leads to the following contribution of the spatial element at *r* to the optical path difference for radiation polarized in π- or σ-polarization [19, 20, 23, 26, 27]:

$$\mathrm{OPD}_{n,\sigma/\pi}(r) = n_{rc/a}'(T(r))\, T(r)\, \Delta\ell(z). \tag{31}$$

Since in the YLF experiment the longitudinal axis is one of the two a-axes of the crystal, the contribution of the spatial element at *r* to the optical path difference induced by end-face bulging is given by [19, 20, 23, 26, 27]

$$\mathrm{OPD}_\alpha(r) = (n_{ra} - 1)(1 + \nu)\, \alpha_{Ta}'(T(r))\, T(r)\, \Delta\ell(z), \tag{32}$$

with α_{Ta}' from eq. (30). In the paraxial approximation, the transverse shape of the optical path difference for a beam traveling in the longitudinal direction is calculated from eqs. (31), (32), and

$$\mathrm{OPD}_{\sigma/\pi}(r) = \sum_{z=1} \mathrm{OPD}_{n,\sigma/\pi}(r) + \mathrm{OPD}_\alpha(r). \tag{33}$$

We fit a value of a spherical lens to each spacing between two transversely adjacent finite elements in order to derive the thermal lens power with transverse resolution. A spherical thermal lens at radial position *r* is described by the equations [58, 59]

$$\mathrm{dOPD}_{\sigma/\pi}(r) = \mathrm{OPD}_{\sigma/\pi}(r) - k_{\sigma/\pi}\, dr^2 / 2, \tag{34}$$

$$f_{\sigma/\pi}(r) = - r / [\ell_c\, \mathrm{dOPD}_{\sigma/\pi}(r) / dr] = 1 / [\ell_c\, k_{\sigma/\pi}]. \tag{35}$$

$f_{\sigma/\pi}$ are the focal lengths for σ- and π-polarization, respectively. In contrast to the commonly used equation $f(r) = -1 / [\ell_c\, d^2OPD(r)/dr^2]$, eq. (35) also describes the thermal lens correctly, if

Acknowledgments

The authors thank Wolfram Schöne from the Laserzentrum Hannover, Germany, for helpful discussions concerning the thermal lens calculations. Parts of the source code were developed during an earlier work at the Institute of Applied Physics, University of Bern, Switzerland. M. Pollnau is supported by a fellowship from the European Union within the "Human Capital and Mobility Programme". P. J. Hardman acknowledges the support of Lumonics, Ltd., in the form of a Cooperative Award in Science and Engineering studentship.

[11] P. J. Hardman, M. Pollnau, W. A. Clarkson, and D. C. Hanna, "Thermal lensing in high-power end-pumped Nd:YLF lasers", in UK National Quantum Electronics Conference QE-13, Institute of Physics Technical Digest, 1997, p. 132.

[12] H. G. Danielmeyer, M. Blätte, and P. Balmer, "Fluorescence quenching in Nd:YAG", Appl. Phys. 1 (?), 269-274 (1973).

[13] D. P. Devor, L. G. DeShazer, and R. C. Pastor, "Nd:YAG quantum efficiency and related radiative properties", IEEE J. Quantum Electron. 25 (8), 1863-1873 (1989).

[14] T. Y. Fan, "Heat generation in Nd:YAG and Yb:YAG", IEEE J. Quantum Electron. 29 (6), 1457-1459 (1993).

[15] V. Lupei and A. Lupei, "Emission quantum efficiency and heating effects in YAG:Nd^{3+} lasers", Opt. Eng. 35 (5), 1252-1257 (1996).

[16] M. Pollnau, W. A. Clarkson, and D. C. Hanna, "Thermal lensing in end-pumped Nd:YAG under lasing and non-lasing conditions", in Conference on Lasers and Electro-Optics, Vol. 6, 1998 OSA Technical Digest Series (Optical Society of America, Washington, D.C., 1998), pp. 100-101.

[17] A. V. Mezenov, L. N. Soms, and A. I. Stepanov, "Thermooptics and solid-state lasers", J. Sov. Laser Res. 8 (5), 427-550 (1987).

[18] M. E. Innocenzi, H. T. Yura, C. L. Fincher, and R. A. Fields, "Thermal modeling of continuous-wave end-pumped solid-state lasers", Appl. Phys. Lett. 56 (19), 1831-1833 (1990).

[19] S. C. Tidwell, J. F. Seamans, M. S. Bowers, and A. K. Cousins, "Scaling CW diode-end-pumped Nd:YAG lasers to high average powers" IEEE J. Quantum Electron. 28 (4), 997-1009 (1992).

[20] A. K. Cousins, "Temperature and thermal stress scaling in finite-length end-pumped laser rods", IEEE J. Quantum Electron. 28 (4), 1057-1069 (1992).

[21] J. Frauchiger, P. Albers, and H. P. Weber, "Modeling of thermal lensing and higher order ring mode oscillation in end-pumped CW Nd:YAG lasers", IEEE J. Quantum Electron. 28 (4), 1046-1056 (1992).

[34] S. Guy, C. L. Bonner. D. P. Shepherd. D. C. Hanna, A. C. Tropper, and B. Ferrand, "High-inversion densities in Nd:YAG: upconversion and bleaching", IEEE J. Quantum Electron. 34 (5), 900-909 (1998).

[35] D. C. Brown. "Ultrahigh-average-power diode-pumped Nd:YAG and Yb:YAG lasers", IEEE J. Quantum Electron. **33** (5), 861-873 (1997).

[36] N. W. Ashcroft and N. D. Mermin, *Solid State Physics* (Sounders College, Philadelphia, 1976, international edition), chapter 25.

[37] G. A. Slack and D. W. Oliver, "Thermal conductivity of garnets and phonon scattering by rare-earth ions", Phys. Rev. B **4** (2), 592-609 (1971).

[38] B. W. Woods, S. A. Payne, J. E. Marion, R. S. Hughes, L. E. Davis, "Thermomechanical and thermo-optical properties of the $LiCaAlF_6:Cr^{3+}$ laser material", J. Opt. Soc. Am. B **8** (5), 970-977 (1991).

[39] W. Koechner, *Solid-State Laser Engineering*, 4th ed., Springer Ser. Opt. Sci., Vol. **1** (Springer-Verlag, Berlin, Heidelberg, New York, 1996), chapter 2.

[40] D. S. Sumida, D. A. Rockwell, and M. S. Mangir, "Energy storage and heating measurements in flashlamp-pumped Cr:Nd:GSGG and Nd:YAG", IEEE J. Quantum Electron. 24 (6), 985-994 (1988).

[41] E. G. Spencer, R. T. Denton, T. B. Bateman, W. B. Snow, and L. G. Van Uitert, "Microwave elastic properties of nonmagnetic garnets", J. Appl. Phys. **34** (10), 3059-3060 (1963).

[42] A. A. Kaminskii, *Laser Crystals*, Springer Ser. Opt. Sci., Vol. **14** (Springer-Verlag, Berlin, Heidelberg, New York, 1981).

[43] P. H. Klein and W. J. Croft, "Thermal conductivity, diffusivity, and expansion of Y_2O_3, $Y_3Al_5O_{12}$, and LaF_3 in the range 77°-300°K", J. Appl. Phys. **38** (4), 1603-1607 (1967).

[44] J. R. Ryan and R. Beach, "Optical absorption and stimulated emission of neodymium in yttrium lithium fluoride", J. Opt. Soc. Am. B 9 (10), 1883-1887 (1992).

[45] J. D. Zuegel and W. Seka, "Direct measurement of $^4I_{11/2}$ terminal-level lifetime in Nd:YLF", IEEE J. Quantum Electron. **31** (10), 1742-1746 (1995).

[58] M. A. Kern, W. A. Clarkson, and D. C. Hanna, "Resonator design considerations for high-power TEM_{00} operation of a Nd:YAG laser at 1.3 μm end pumped by a diode bar", in Conference on Lasers and Electro-Optics, Vol. **11**, 1997 OSA Technical Digest Series (Optical Society of America, Washington, DC 1997), pp. 479-480.

[59] M. A. Kern, "Resonator design considerations for a high-power end-pumped Nd:YAG laser operating at 1.3 μm", M.S. thesis, Institute of Laser-Physics, University of Hamburg, Germany, 1997.

Table 2. Spectral distributions of the diode pump power in the experiments investigating Nd:YLF (upper 8 rows) and Nd:YAG (lower 5 rows)

No.	$\lambda(i)$ [nm]	$P_{in,\lambda(i)} / P_{in}$ [%]	$\sigma_{p,\lambda(i)}$ [10^{-20} cm^2]	$\sigma_{s,\lambda(i)}$ [10^{-20} cm^2]
1	798.8	6.1	3.30	3.85
2	799.2	8.6	2.40	2.80
3	799.5	14.4	2.10	2.40
4	799.9	20.9	1.85	2.00
5	800.3	20.9	1.75	1.85
6	800.7	14.4	1.70	1.75
7	801.0	8.6	1.70	1.70
8	801.4	6.1	1.75	1.70
1	808.0	16	2.6	-
2	808.5	21	3.3	-
3	809.0	26	4.6	-
4	809.5	21	2.0	-
5	810.0	16	1.3	-

Table 4. Parameters of the laser transitions in Nd:YLF and Nd:YAG

Crystal	YLF			YAG	
Polarization	π-pol	σ-pol	Ref.		Ref.
Upper Stark laser level	2	1	[44]	2	[50]
Lower Stark laser level	3	3		3	
Wavelength λ_l [nm]	1047	1053		1064	
Boltzmann factor b_4 (300 K)	0.427	0.573		0.384	
Boltzmann factor b_l (300 K)	0.113	0.113		0.186	
Eff. emission cross-section [10^{-19} cm^2]	1.9	1.4		4.6	
Atomic cross-section σ_{em} [10^{-19} cm^2]	4.45	2.44		12.0	
Degeneracy g_4	2	2		2	
Degeneracy g_l	2	2		2	
Fraction P	10^{-11}	10^{-11}		10^{-11}	
Optical resonator length ℓ_{opt} [mm]	136	136	Exp.	143	Exp.
Double-pass losses L [%]	1.0	1.0		1.8	
Mirror reflectance in / out Rf [%]	100 / 90	100 / 90	Exp.	100 / 97	Exp.
TEM$_{00}$ laser-beam radius w_l [μm]	300	300	Exp.	200	Exp.

Table 6. Values of the parameters used for the calculation of the temperature profiles and thermal lenses in YLF and YAG. The temperature dependence of the YLF values denoted with an asterisk are estimated from the corresponding dependence in YAG.

Crystal	YLF			YAG	
Axis	c-axis	a-axis	Ref.		Ref.
Thermal conductivity					
K_C (300 K) [W K^{-1} m^{-1}]	5.8	7.2	[38]	12	averaged
T-independent Θ [W m^{-1}]	1740	2160		3600	
Temp. of radial heat sink T_{br} [K]	288		Exp.	288	Exp.
Transfer coeff. Cu K_{Tr} [W m^{-2}]	1×10^4			1×10^4	[20,26,27]
Temp. of long. heat sink T_{bz} [K]	293		Exp.	293	Exp.
Transfer coeff. air K_{Tz} [W m^{-2}]	6.5			6.5	[52]
Refractive index n_r	1.470	1.448	[23,39]	1.82	[23,24,39,42]
$dn_r/dT = n_r'$ (300 K) [10^{-6} K^{-1}]	−4.3	−2.0	[2,23,38]	8.3	[24]
$dn_r'/dT = n_r''$ [10^{-8} K^{-2}]	−1.3 *	−0.63 *		2.6	[24]
Expansion coeff.					
α_T' (300 K) [10^{-6} K^{-1}]	8	13	[2,23,38,39]	5.8	[35]
$d\alpha_T'/dT = \alpha_T''$ [10^{-8} K^{-2}]	1.73 *	2.82 *		1.25	[35]
Scaling factor C_α	0.35			0.35	
Poisson's ratio ν	0.33		[23,39]	0.25	[35]

Fig. 5. Calculated thermal power dissipated in the whole crystal versus absorbed pump power under non-lasing and lasing conditions for Nd:YLF (thick lines) and Nd:YAG (thin lines). The data under non-lasing conditions are not directly comparable, because the pump-waist areas are 340 μm x 220 μm in Nd:YLF and 225 μm × 225 μm in Nd:YAG, leading to a different influence of upconversion under non-lasing conditions.

Fig. 6. Calculated temperature profiles for Nd:YLF versus sagittal radius (pump-beam radius w_{py0} = 220 μm, laser-beam radius w_{ly} = 300 μm) under (a) non-lasing and (b) lasing conditions. The radial boundary given by the rod radius is $r_b = \pm 2$ mm. Owing to convective radial cooling by a water-cooled copper block the temperature at the boundary is elevated from the radial coolant temperature of T_{br} = 288 K by a few K.

Fig. 7. Nd:YLF: (a) Dioptric power of the thermal lens versus incident pump power along the crystal a-axis and (b) variation of dioptric power (spherical aberration) of thermal lensing versus radius along the crystal a-axis at the highest incident pump power of 12 W: experimental data (solid symbols), taken from Ref. [11], and calculated data (open symbols), in σ-polarization under non-lasing (squares) and lasing (triangles) conditions as well as in π-polarization under non-lasing (diamonds) and lasing (circles) conditions.

Fig. 8. Nd:YAG: (a) Dioptric power of the thermal lens versus incident pump power and (b) variation of dioptric power (spherical aberration) of thermal lensing versus radius at the highest incident pump power of 14.2 W: experimental data (solid symbols), taken from Ref. [16], and calculated data (open symbols), under non-lasing (squares) and lasing (triangles) conditions.

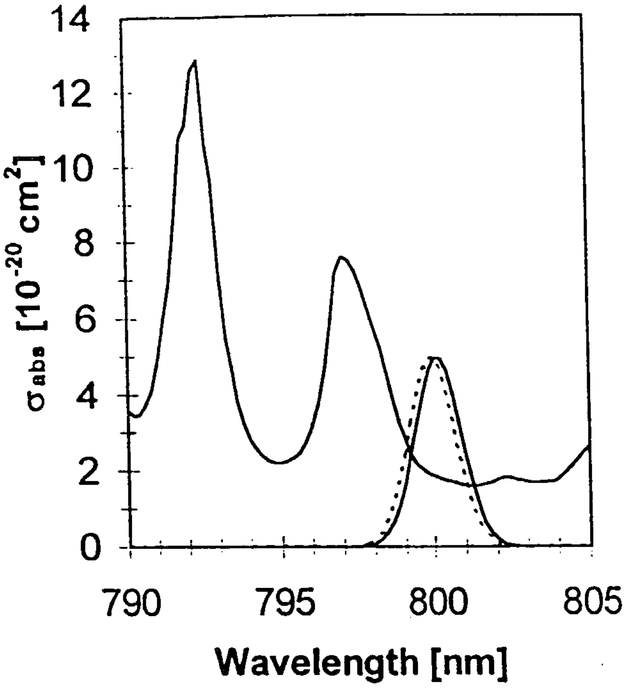
14
12
10
8
6
4
2
0
σ_{abs} [10^{-20} cm^2]
790
795
800
805
Wavelength [nm]

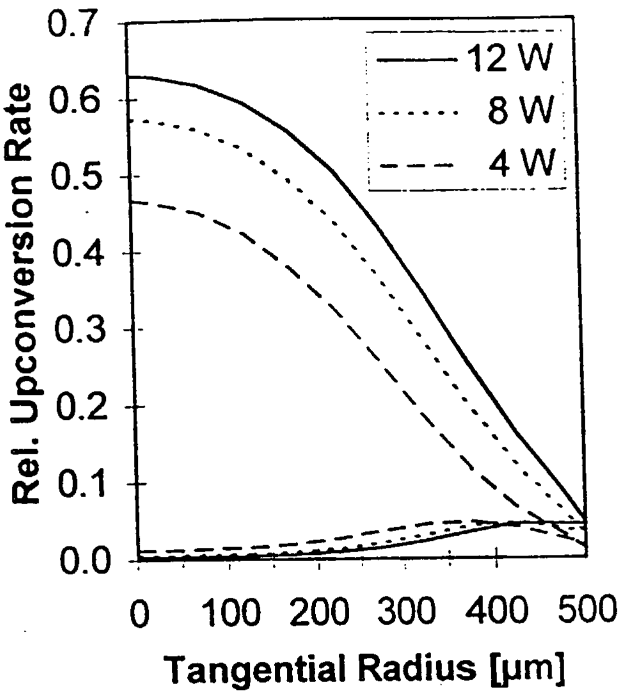
0.7
0.6
0.5
0.4
0.3
0.2
0.1
0.0
Rel. Upconversion Rate
12 W
8 W
4 W
0
100
200
300
400
500
Tangential Radius [μm]

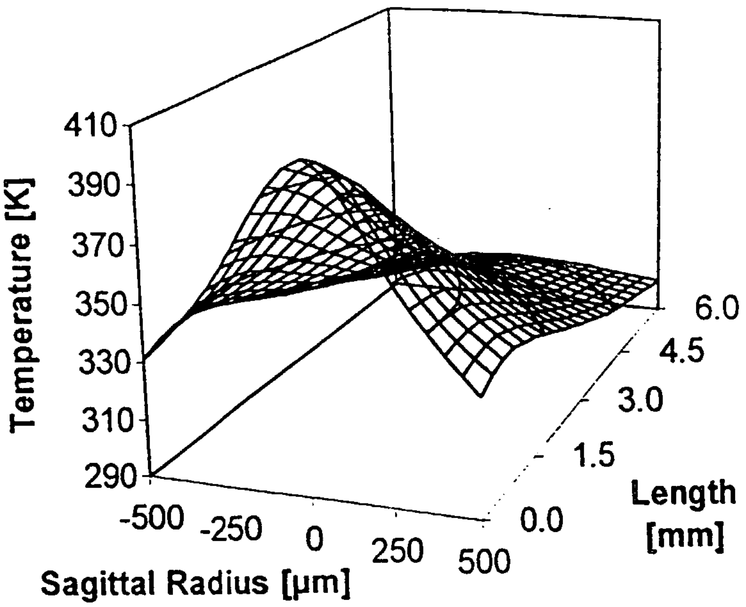
Temperature [K]
410
390
370
350
330
310
290
-500
-250
0
250
500
Sagittal Radius [µm]
0.0
1.5
3.0
4.5
6.0
Length [mm]

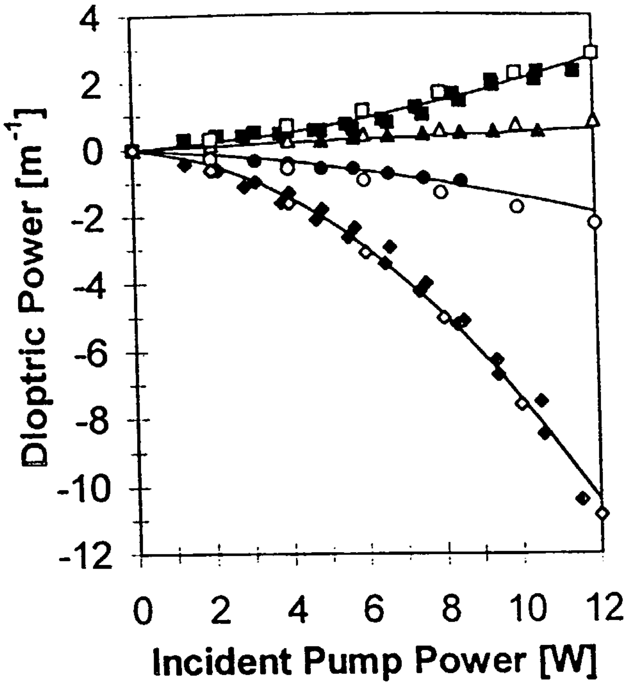
4
2
0
-2
-4
-6
-8
-10
-12
Dioptric Power [m^{-1}]
0
2
4
6
8
10
12
Incident Pump Power [W]

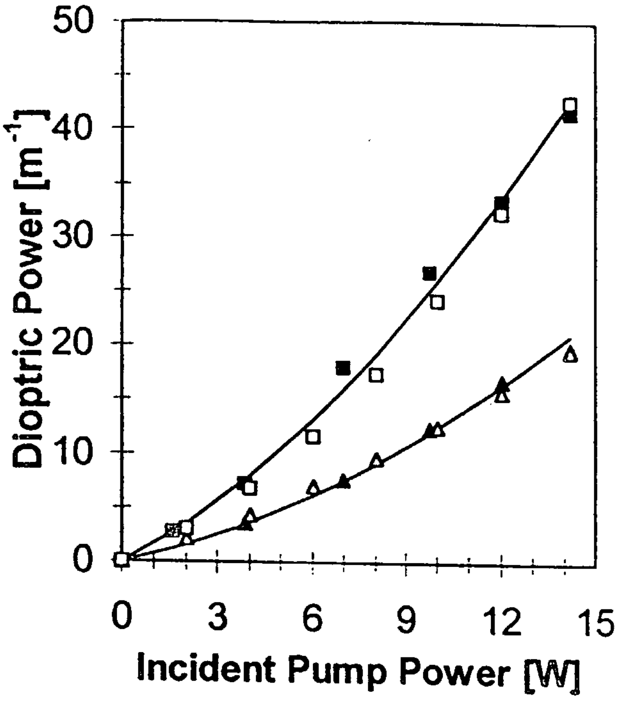
Dioptric Power [m^{-1}]
50
40
30
20
10
0
0
3
6
9
12
15
Incident Pump Power [W]